Electronic Supplementary Material (ESI) for Chemical Science.
This journal is © The Royal Society of Chemistry 2020

Supplementary Information for:

A Critical Analysis of Electrospray Techniques for the Determination of Accelerated Rates and Mechanisms of Chemical Reactions in Droplets

Grazia Rovelli,[a] Michael I. Jacobs,[a,b,#] Megan D. Willis,[a] Rebecca J. Rapf,[a,§] Alexander M. Prophet[a,b] and Kevin R. Wilson*,[a]

[a] Chemical Sciences Division, Lawrence Berkeley National Laboratory, Berkeley, 94720, CA, USA.

[b] Department of Chemistry, University of California, Berkeley, 94720, CA, USA.

[#] Now at: Beckman Institute, University of Illinois, 61801, Urbana-Champaign, IL, USA.

[§] Now at: Department of Chemistry, Trinity University, San Antonio, 78212, TX, USA.

Table of Contents:

S1. Modelling simultaneous evaporation and reaction of methanol-phenylhydrazine-isatin droplets

The evaporation of ternary methanol-phenylhydrazine-isatin droplets is simulated by integration of the Maxwell equation for evaporation:[1]

$$r^2 = r_0^2 - \frac{2D_i M_i p_i^0(T)}{\rho_i R T}(t - t_0) \qquad \text{Eq. S1}$$

where r^2 and r_0^2 are the radius squared as a function of time (t) and at time zero (t_0), D_i is the diffusion coefficient of the evaporating species i into the gas phase (assumed to be pure nitrogen in this work), $p_i^0(T)$ is the pure component vapor pressure of i at temperature T, ρ_i is the density of the species i, and R is the gas constant.

With the aim of keeping the simulation of droplet evaporation simple yet realistic, a series of assumptions are required. The main approximation is related to evaporative cooling. When rapid evaporation of solvent occurs (as in the case of methanol evaporating from electrosprayed droplets) the latent heat of vaporisation is supplied to the evaporating molecules, which decreases the surface temperature of the droplets.[1] In turn, evaporative cooling causes a partial suppression of the effective vapor pressure of the evaporating species and therefore a slower evaporation rate than expected and described by Eq. S1. However, Gregson and coworkers[2] showed that the evaporation of a pure ethanol droplet into dry nitrogen can be satisfactorily modelled using Eq. S1 by assuming a droplet surface temperature that is equal to the wet bulb temperature of ethanol (276 K). We demonstrate the validity of this assumption by comparing our simulations against the experimental measurement of a pure ethanol droplet evaporation into dry nitrogen (data from Gregson et al.,[2]

Figure S1). For this reason, in this work the evaporation of methanol is evaluated at its wet bulb temperature (264 K) in order to account for evaporative cooling.

Phenylhydrazine is semi-volatile (vapor pressure of 3.43 Pa at 298 K).[3] The effect of evaporative enrichment on the acceleration of the isatin/phenyl hydrazine reaction rate is evaluated both by considering isatin is involatile (Figure 3 in the main manuscript) and by including the evaporation of isatin (Figure S3). In Figure S3, the evaporation of isatin is also modelled with Eq. S1. The vapor pressure of isatin is low enough (and therefore its evaporation is slow enough) to allow evaporative cooling caused by its evaporation to be negligible.

In addition to the main approximation on the treatment of evaporative cooling, the following simplifications are also applied:

1. The evaporation of methanol and phenyl hydrazine (in the "volatile reagents" case) are decoupled. This means that methanol is allowed to evaporate first and then the evaporation of phenylhydrazine is 'turned on'. This is reasonable given the large differences in vapor pressure of these compounds (See Section S2). If the two reagents were allowed to evaporate simultaneously, the calculated droplets lifetime would be shorter than estimated in Figure S2.
2. The Kelvin effect is neglected because it would affect only droplets smaller than 100 nm in radius, which are present in very small numbers and only in one of the considered size distributions. The small increase in vapor pressure due to the Kelvin effect would not significantly affect the overall distribution of products and reagents both in the gas and in the condensed phase.

3. The evaporation is assumed to be gas-diffusion controlled and thus Stefan flow (i.e. the convective motion associated with vapor transport from the surface) is not considered because the modelled droplets are far from the boiling point of their components.[1]
4. The effect of charge on evaporation and the Coulombic explosion that occurs when ESI/ESSI droplets reach the Rayleigh limit is neglected in the evaporation model. Tang and Kebarle[4] proposed a description of this phenomenon. We have used their description of the fission events occurring with evaporating electrosprayed droplets, which assumes that once a droplet reaches 80% of its Rayleigh limit it generates 20 offspring droplets, each characterised by 10% of the radius of the parent droplet and the 0.75% of its initial charge. The extent to which this phenomenon is found to accelerate the evaporation of pure methanol droplet (r_0 = 1000 nm) is shown in Figure S4. Accounting for this results in a minor decrease in the overall parent droplet lifetime from ~0.7 ms to ~0.66 ms. For this reason, this process has not been included in the modelling approach used in this work. However, the fission process is important because it accelerates the transfer of reagents to the gas phase; the implications of which are discussed in Sections 4.2 and 4.5 of the main manuscript.
5. The model does not take into account the vapor pressure depression from solutes and that a slight dependence of the methanol evaporation timescale as a function of the initial concentration in the droplets should be expected. However, this effect is minor and does not change the overall conclusions drawn from Figures 3, 4, 5 and S3.
6. At each time point during the evaporation, the droplet's condensed phase is considered to be ideal. Our modelling approach assumes that the evaporating droplets are homogeneous

throughout the simulations and we have not examined the possible occurrance of liquid-liquid phase separation.

7. The model simulates the evaporation of a droplet into a stagnant gas-phase, whereas ESI/ESSI droplets are rapidly moving either through ambient air or a desolvation gas flow (ESI), or through a flowing nebulizer gas (ESSI). Droplet movement through the surrounding gas-phase enhances the rate of mass transfer from an evaporating droplet to the gas-phase, further accelerating solvent evaporation. Accounting for this effect is typically done by scaling the modelled mass transfer by the Sherwood number.[1] This calculation for ESI/ESSI droplets plumes would be quite complicated since there are a number of unknowns, such as the relative velocity of the droplets and carrier gas (which might not be uniform throughout the travel distance to the MS inlet and dependent on droplet size, see Section 4.5). Since the motion of droplets through the gas-phase is that of enhancing the rate of mass transfer from an evaporating droplet to the gas-phase, all the modelling results presented in this work are upper limits for the real evaporation timescale.

S2. Parameters in Eq. S1 used in the modelling of ethanol, methanol, water and phenyl hydrazine evaporation.

	Ethanol	
	T = 293 K	*T = 276 K*
p^0 / kPa	5.774 (a)	1.9 (a)
D / m^2 s^{-1}	$1.13 \cdot 10^{-05}$ (b)	$1.02 \cdot 10^{-05}$ (c)
ρ / kg m^{-3}	789 (d)	804 (d)

(a) Lange's Handbook of Chemistry.[5]

(b) Calculated with Chapman-Enskog theory.[6]

(c) Temperature dependence of D from Fuller's method from Tang et al. (2015).[7]

(d) Dortmund Data Bank, 2020, www.ddbst.com.

	Methanol	
	T = 293 K	*T = 266 K*
p^0 / kPa	12.810 (a)	2.472 (a)
D / m^2 s^{-1}	$2.02 \cdot 10^{-05}$ (b)	$1.66 \cdot 10^{-05}$ (c)
ρ / kg m^{-3}	792 (d)	816 (d)

(a) Lange's Handbook of Chemistry.[5]

(b) Calculated with Chapman-Enskog theory.[6]

(c) Temperature dependence of D from Fuller's method from Tang et al. (2015).[7]

[d] Dortmund Data Bank, 2020, www.ddbst.com.

	Water	
	T = 293 K	*T = 279 K*
p^0 / kPa	2.317 [a]	0.939 [a]
D / $m^2 s^{-1}$	$2.45 \cdot 10^{-05}$ [b]	$2.25 \cdot 10^{-05}$ [b]
ρ / kg m^{-3}	998.2 [c]	999.9 [c]

[a] Murphy and Koop (2005).[8]

[b] Massman (1998).[9]

[c] CRC Handbook of Chemistry and Physics.[10]

	Phenyl hydrazine
	T = 293 K
p^0 / kPa	0.00343 [a]
D / $m^2 s^{-1}$	$1.22 \cdot 10^{-05}$ [b]
ρ / kg m^{-3}	1098 [c]

[a] Yaws (1994).[10]

[b] Calculated with Chapman-Enskog theory.[6]

[c] The Merck Index - An Encyclopedia of Chemicals, Drugs, and Biologicals (2001).[11]

S3. Velocity and size distribution of ESI, nESI and ESSI droplets

A significant uncertainty in the determination of reaction kinetics in ESI, nESI and ESSI droplets is the reaction timescale, which is normally controlled by varying the distance between the emitter and the inlet of the mass spectrometer. Converting distance to reaction time requires droplet velocity. Whereas measuring the distance between the emitter tip and the mass spectrometer is straightforward, measuring or estimating the droplets velocity is not. This is because velocity will depend on droplet size, ESI flow rate, emitter tip size,[12] coaxial gas pressure (if present) and distance (i.e. the velocity might not remain constant during their transit time to MS[13,14]). There is further complexity in observing small and fast-moving objects.

ESI, nESI and ESSI droplet velocities are generally measured either by high-speed cameras[15,16] or with phase Doppler anemometry.[14,17,18] With high-speed cameras[15,16] one simply takes successive frames and measures the distance travelled for a single droplet between each frame. From the camera frame rate, velocity can be determined. The diameter of a droplet is directly inferred from the image itself and the limit of detection (i.e. the smallest droplets that can be detected with a certain setup) is determined by the spatial resolution of the camera. Doppler anemometry[14,17,18] (also referred to as interferometry of velocimetry) measures the Doppler shift, between the incident light from a set of lasers and the scattered light by the plume of droplets, which is proportional to velocity.

Lee et al.[15] used a high-speed camera to determine both the droplet's velocity and size in their ESSI microdroplet fusion mass spectrometry setup. They reported a velocity of 84 ± 18 m/s for aqueous droplets of 13 ± 6 µm in diameter (emitter inner diameter 100 µm, flow rate of 30 µL/min and coaxial gas at 120 psi, statistics on 243 droplets). Qualitative comparisons between the work of Lee et al.[15] and other studies on the size and the velocities of ESSI and ESI droplets can provide useful insights about the nature of the spray plumes and its effects on the observed acceleration of reaction rates in aerosol droplets. It must be noted that such comparisons are necessarily qualitative, since the exact characteristics of droplets formed in ESI and ESSI depend on the specific experimental conditions.

Using Doppler anemometry Olumee et al.[14] showed that 90/10% methanol/water ESSI droplets (diameter up to ~5 μm, 150 μm capillary inner diameter, 4 kV applied voltage, 24 μL/min flow rate) have a distribution of velocities, that peak at 30 m/s at 4 mm from the sprayer tip and decreases to 10 m/s at a distance of 22 mm. Nemes et al.[17] showed that for 50/50% methanol/water the droplet size changes as a function of the "spraying mode" (in other words, how stable the spray is), with broader distributions and larger droplets formed under less stable spraying conditions. They measured velocities ranging from 1 to 6 m/s at 13 mm from the emitter tip, with larger droplets travelling faster than smaller droplets. Furthermore, calculations from Stindt et al.[16] indicate that for an ESSI source the velocity of the produced droplets is 25-50 times slower than the supersonic velocity of the coaxial gas velocity. Based on this, with a typical gas velocity of Mach 1 (343 m/s in dry air at 293 K), one can therefore make a reasonable estimate of droplet velocities to be ~6-14 m/s. These velocities are about one order or magnitude smaller than what is reported by Lee et al.[15]. It is possible that Lee et al.[15] are measuring a velocity of 84 ± 18 m/s for the larger droplets their camera is able to detect and not capturing slower velocities for the smaller droplets that are below the detection limit of their camera and optical system. Additionally, applying Doppler anemometry, Smith et al.[19] measured a very broad size distribution from 5 to 45 μm in diameter for aqueous 10^{-4} M NaCl ESI droplets (50 μm emitter tip, 0.2-1 μL/min flow rates), which is much broader than reported by Lee et al.[15] (13 ± 6 μm droplets). There is no mention of the spatial resolution of the camera setup used in the work of Lee et al.[15] and there is no comment on the possible formation of very small droplets that could be below their camera resolution. This qualitative comparison could indicate that this may well be the case.

In a successive publications from Zare and coworkers,[20,21] nESI velocities and droplet sizes from a theta emitter were characterised by means of microparticle imaging velocimetry. Droplet diameters were observed to be in the range 1.3-6.1 μm with velocities in the 8-23 m/s range. In this work, given the resolution of the camera, a lower detection limit for droplet diameter is 1.3 μm, which corresponds to droplets giving a signal of a single pixel.

The nESI experiments in Bain et al. (2016)[22] and Marsh et al. (2019)[23] assume a 6 m/s droplet velocity previously measured from paper sprayed droplets,[24] based on the assumption, that in the absence of a coaxial sheath gas flow, the two ionisation techniques should produce similar droplets velocities. It is unclear whether this is a valid assumption, since the generation of droplets with nESI and paper spray are achieved using quite different means. However, a velocity of 6 m/s is consistent with other measurements on nESI droplets[20,21] and to the measurement by Nemes et al.[17].

An alternative interesting method to measure droplet timescales has been implemented by van Geenen et al.[13] using a laser ablation setup. The time interval between a laser pulse and the first signal measured at the mass spectrometer is measured as a function of the distance between the ESI emitter tip and the MS inlet. This in turn reflects the time necessary for the droplets to reach the inlet, and therefore the reaction time. From the data reported in Figure 2C in Geenen et al.[13], velocities decreasing from 6 m/s to 1 m/s (1 m from the emitter tip) are estimated for 1:1

methanol/water ESSI droplets (5 μL/min flow rate, 1 L/min coaxial sheath gas flow). This result is remarkably close to what was reported by Nemes et al.[17] and mentioned above.

This brief overview of the literature (though possibly not exhaustive) provides a fair picture of the typical assumptions and uncertainties related to the measured or estimated velocity of ESI, nESI and ESSI droplets. Usually, acceleration factors are estimated by calculating the ratio of the timescales at which equal amounts of product are formed from the same reaction in the bulk vs. in-droplet. In the light of the above discussion, we can conclude that the estimated reaction timescales and the derived acceleration factors from such experiments can be affected by: 1) uncertainty in droplet velocity, 2) different reaction timescales for different droplets sizes (due to the variable distribution of velocities for smaller and larger droplets)[17]. An overestimate of droplet velocity by one order of magnitude results in a one order of magnitude uncertainty in the reaction timescale and therefore a factor of 10 in the computed acceleration factors.

S4. Trend of acceleration factors as a function of droplet size

The acceleration factors in Figure 3(d), 4(b) and S4(d) do not immediately reach a constant value after the evaporation of methanol is complete but tend to a constant value over timescales that depend on the droplet size. As an example to explain why this kind of trend is observed, we consider the smallest and the largest initial droplets diameters (200 and 4000 nm) in Figure 3. We note that this explanation is also applicable to the data in Figure 4(b) and S4(d). In the table below we select three conversion ratios values (0.0005, 0.002 and 0.004) for the two droplet initial sizes.

Initial diameter = 200 nm

Conversion ratio in droplet	Time / ms	Conversion ratio in bulk	Acceleration factor
0.0005	2.27	$9.99\cdot10^{-7}$	500.50
0.002	9.08	$3.99\cdot10^{-6}$	501.25
0.004	18.08	$7.95\cdot10^{-6}$	503.14

Initial diameter = 4000 nm

Conversion ratio in droplet	Time / ms	Conversion ratio in bulk	Acceleration factor
0.0005	4.97	$2.19\cdot10^{-6}$	228.31
0.002	11.77	$5.18\cdot10^{-6}$	386.10
0.004	20.86	$9.18\cdot10^{-6}$	435.73

The same conversion ratio in the two droplets is reached at earlier times by the smaller droplet, because the evaporation of methanol is complete at earlier timescales for smaller sizes (see Figure 3a). In the table above we are also reporting the conversion ratio for the same reaction conducted in the bulk solution at the corresponding time. The reason why the acceleration factor for the largest droplet is increasing over time after the evaporation of methanol is complete is that when the neat reagents concentration of 5 M is reached at earlier timescales (in the case of the 200 nm droplet) the corresponding conversion ratio for the reaction in the bulk solution is smaller, and therefore the resulting acceleration factor is larger. Conversely, when the 5 M concentration is reached after a longer period (i.e. for the 4000 nm diameter droplet), the bulk has proceeded further reaching a slightly higher conversion ratio, resulting in smaller acceleration factors for the 4000 nm droplet compared to the 200 nm droplet.

Figures:

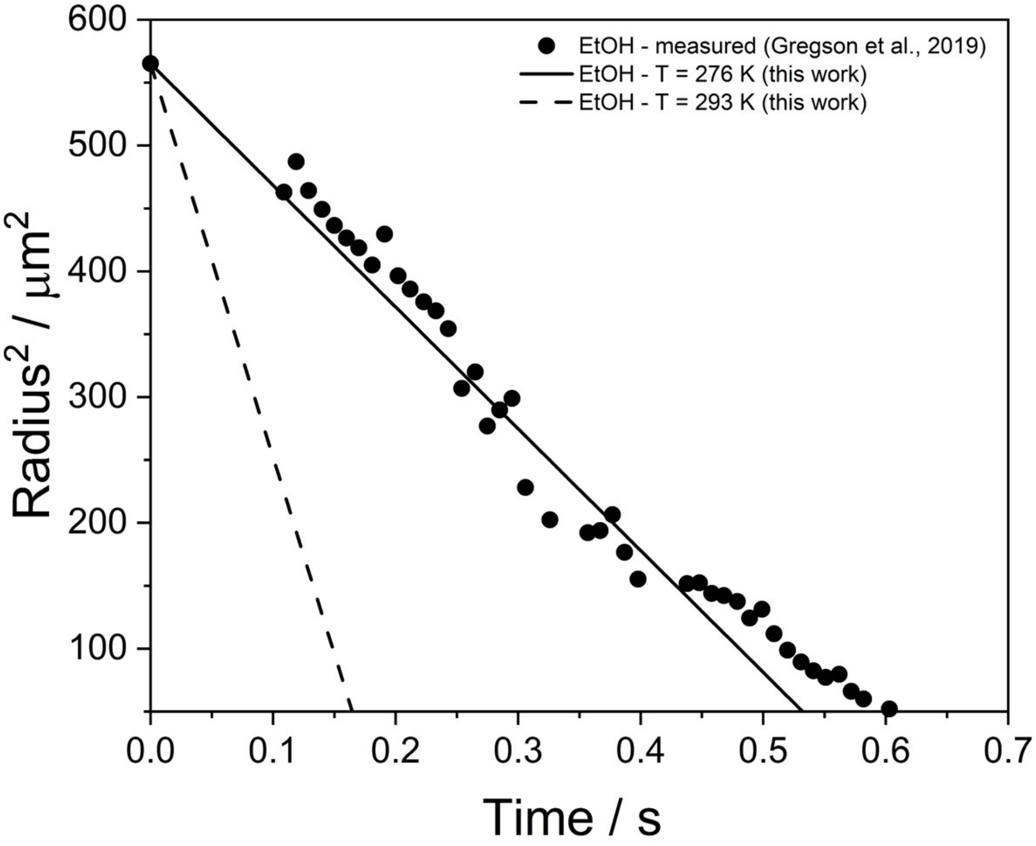

Figure S1: Validation of the modelling approach (Eq. S1) against experimental data on the evaporation of a pure ethanol droplet evaporating into dry nitrogen at 293 K. Simulation at 293 K (not accounting for evaporative cooling, dashed line) and at 276 K (wet bulb temperature of ethanol, solid line). The parameters used in these calculations are reported in Section S2.

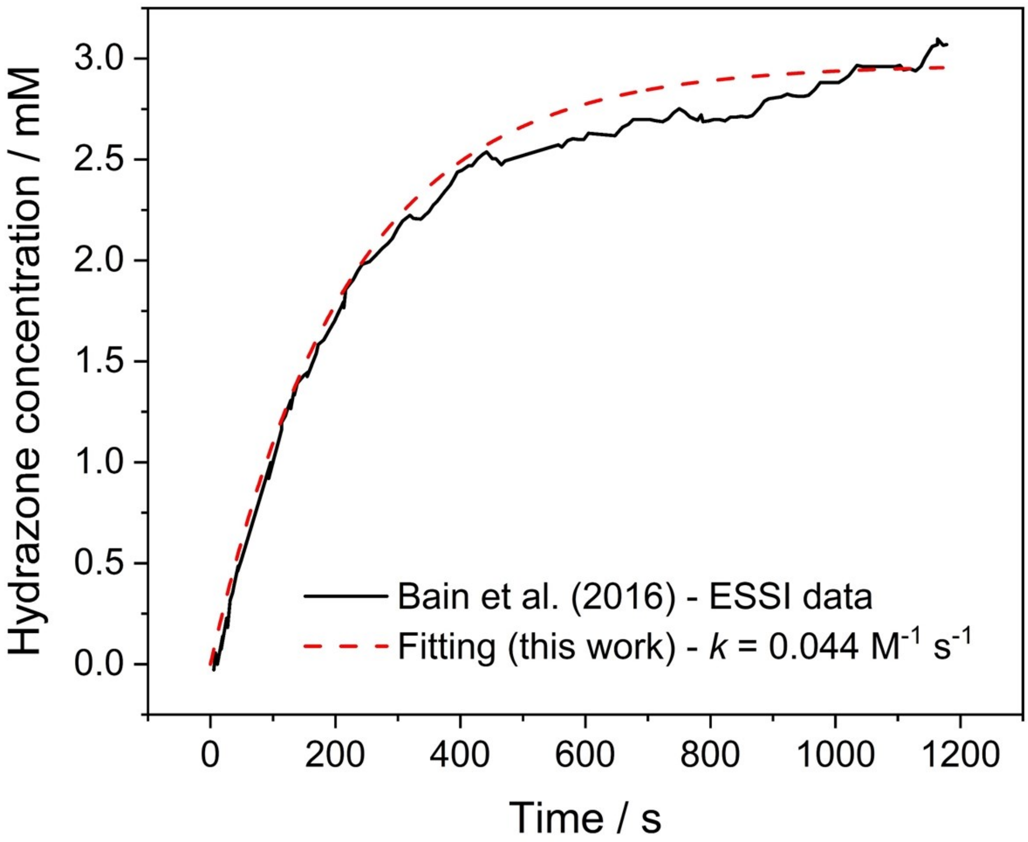

.

Figure S2: Hydrazone product formation vs. time in the bulk ESSI experiments in Bain et al.[25] *(Figure 1b in their work) and best fit (k = 0.044* M^{-1} s^{-1}*) obtained from Eq. 3 in the main manuscript.*

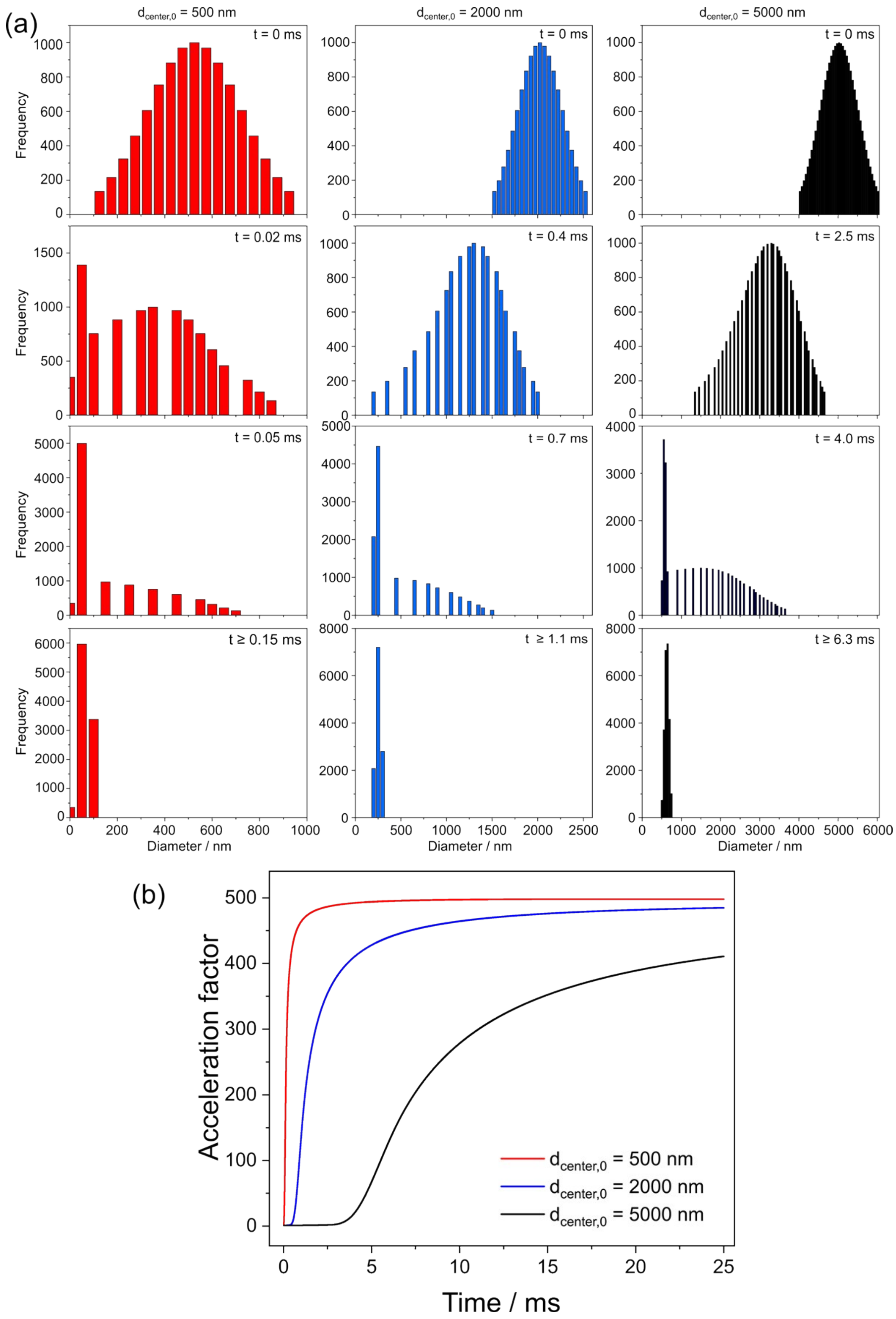

Figure S3: (a) Temporal evolution of the size distribution for three droplets plumes with initial size distributions centered at a diameter $d_{center,0}$ of 500 nm (red), 2000 nm (light blue) and 5000 nm (black), with initial reactants concentrations of 10 mM. (b) Acceleration factor for the same three cases in (a), calculated as in Figure 3 in the main manuscript.

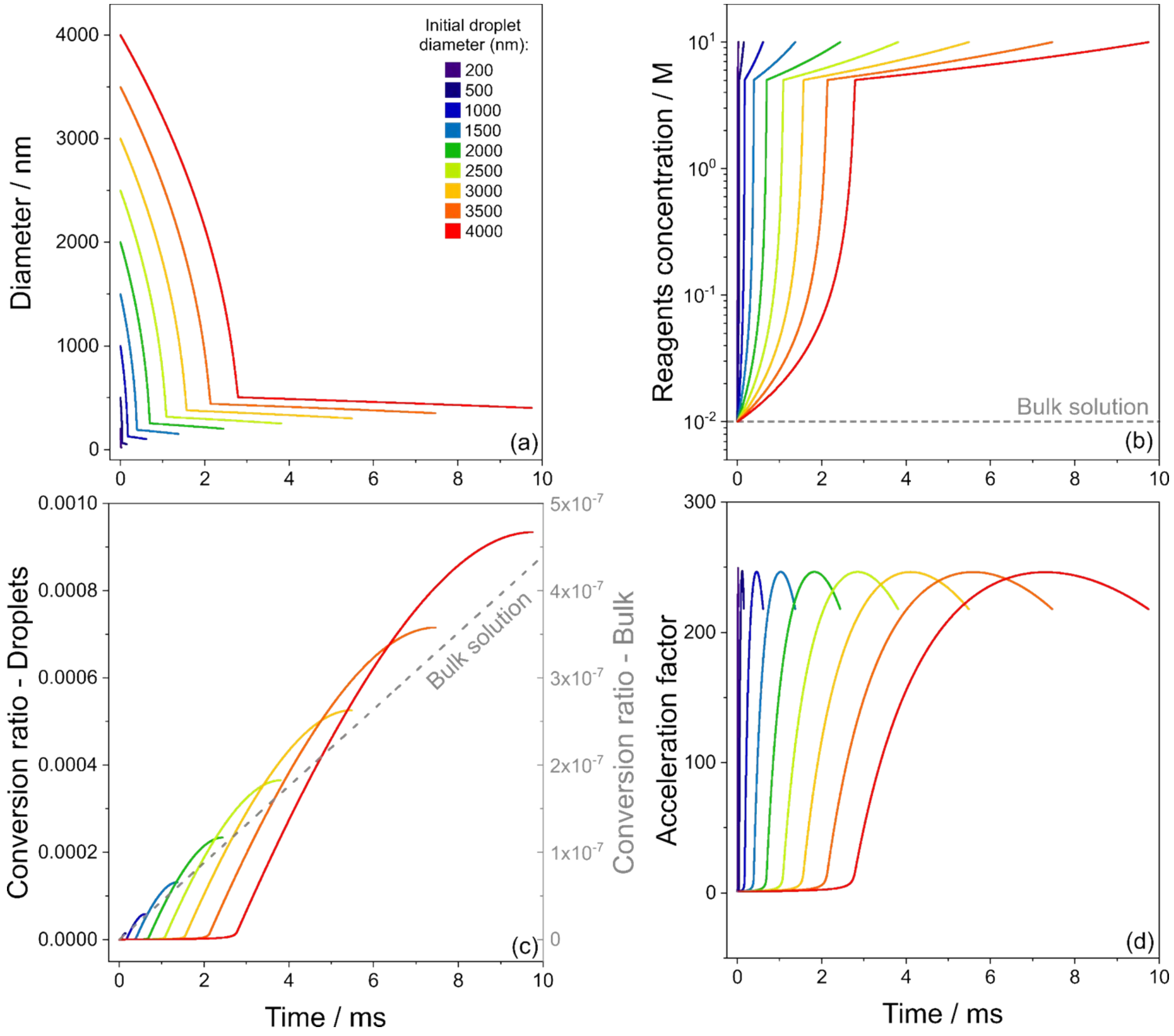

Figure S4: Evaporation of methanol droplets containing isatin and phenyl hydrazine (initial equimolar concentrations of 10 mM), calculated with Eq. (1), and simultaneous reaction (Eq. (3)). Time evolution of droplet diameter (a), concentration of isatin (b), product conversion ratio (c) calculated acceleration factor and (d) for droplets with initial diameters of 200-4000 nm (purple to red color scale). Acceleration factors are calculated dividing the conversion ratio in droplets and that in the bulk solution from panel (c) at each point in time. As opposed to Figure 3 in the main manuscript, here phenyl hydrazine is considered volatile, whereas isatin and the hydrazone product are non-volatile. Due to the evaporation of phenyl hydrazine, the trends for conversion ratio (panel c) and acceleration factors (panel d) differ from those in Figure 3 of the main manuscript. As phenyl hydrazine evaporates, its concentration in solution decreases and the rate of reaction is decreasing over time, too. This can be seen in in panel (c), where the conversion ratio for each droplet becomes flat at the very end of the droplet evaporation. This is what causes the small decrease in acceleration factor at the end of the evaporation in panel (d): the conversion ratio for the bulk solution is continuously increasing, whereas that for the droplets it has reached a constant value, causing the ratio between the two (i.e. the acceleration factor) to decrease slightly.

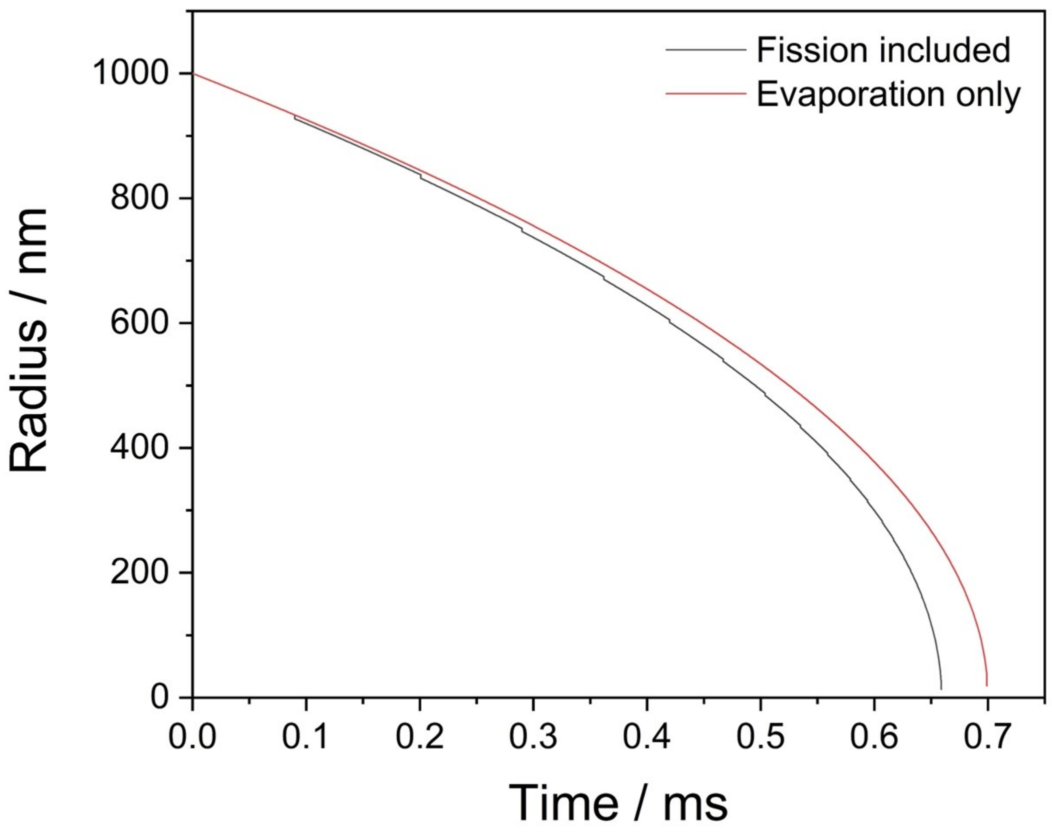

Figure S5: Evaporation of a pure methanol droplet (red, r_0 = 1000nm, calculated with Eq. S1) with no fission events, compared to the evaporation profile of a droplet with the same initial size that undergoes repeated fission events (black) as described in Section S1. Fission events correspond to the points in time where the droplet size changes in steps, because of emission of progeny droplets.

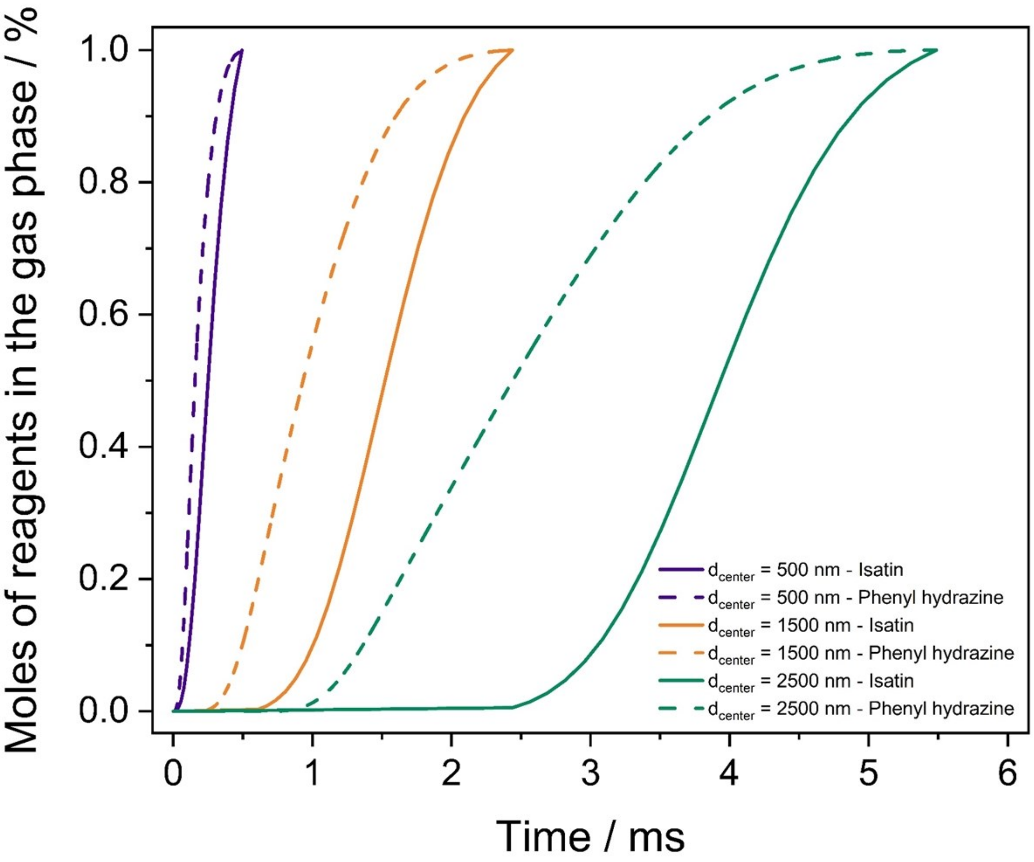

Figure S6: Mole percent of isatin and phenyl hydrazine in the gas-phase for three size distributions with initial central diameters of 500 (purple), 1000 (orange) and 1500 nm (green), with initial concentration of 10 mM. Dashed lines refer to phenyl hydrazine and solid lines to isatin. Phenyl hydrazine evaporates more rapidly than isatin because it is volatile (see discussion in Section 4.3 of the main manuscript).

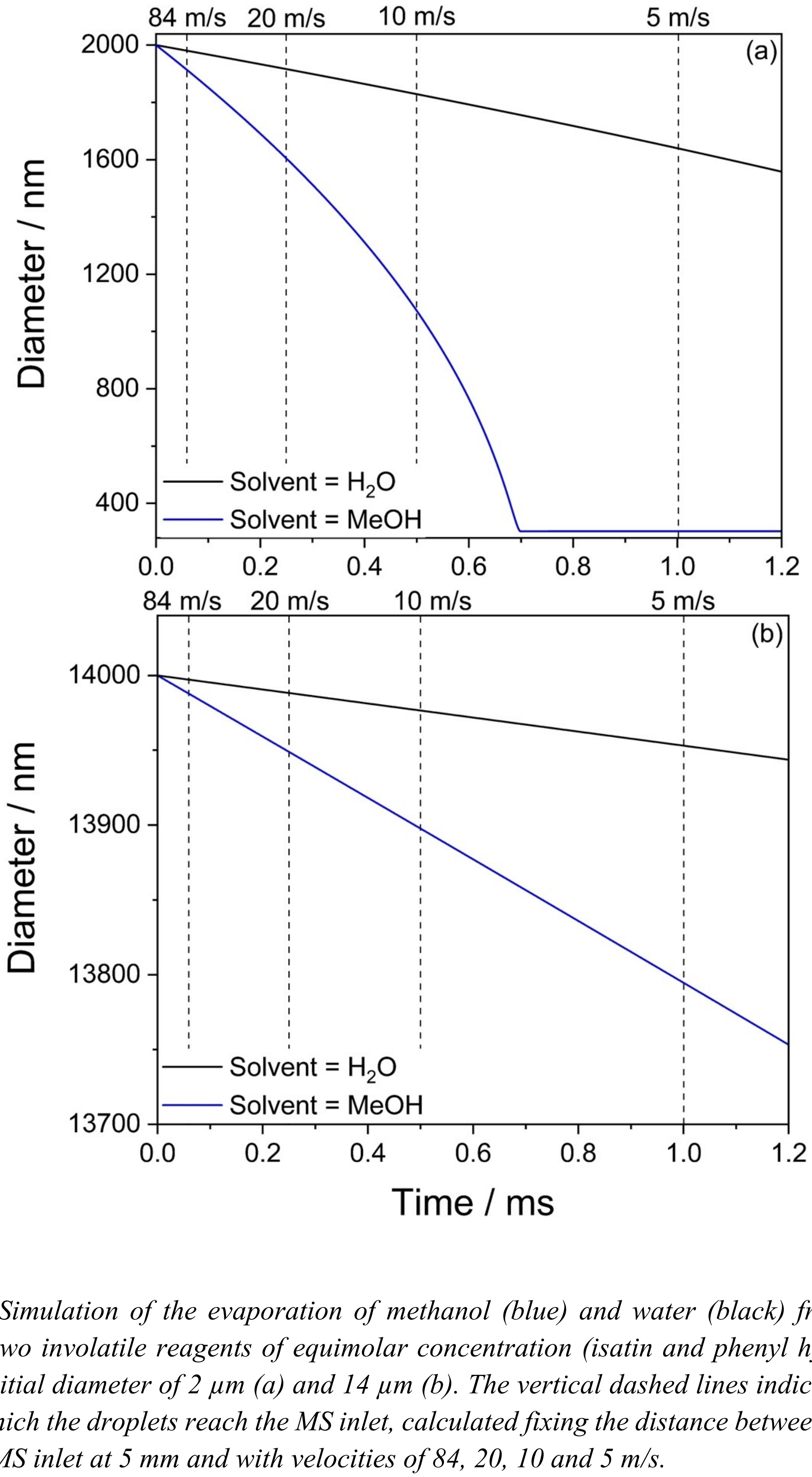

Figure S7: Simulation of the evaporation of methanol (blue) and water (black) from droplets containing two involatile reagents of equimolar concentration (isatin and phenyl hydrazine, 10 mM) with initial diameter of 2 µm (a) and 14 µm (b). The vertical dashed lines indicate the point in time at which the droplets reach the MS inlet, calculated fixing the distance between the emitter tip and the MS inlet at 5 mm and with velocities of 84, 20, 10 and 5 m/s.

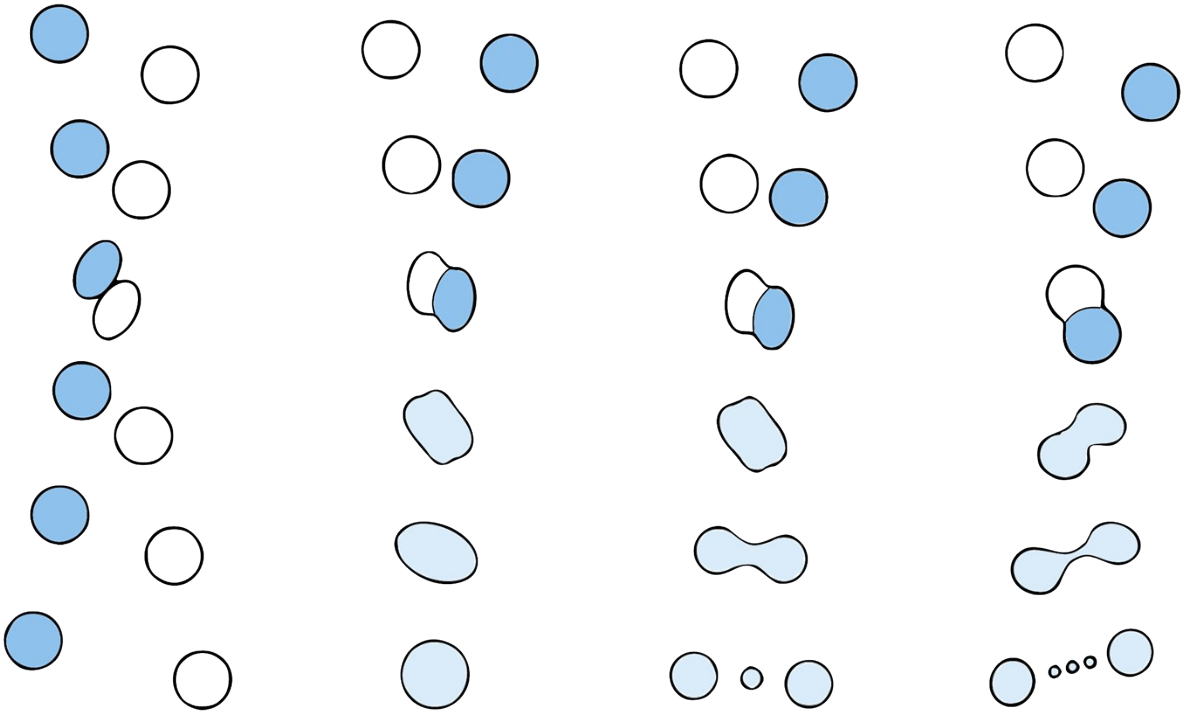

1) Bouncing

2) Coalescence

3) Reflexive separation

4) Stretching separation

Figure S8: Four possible outcomes for the collision of two droplets.[11] *Reprinted from International Journal of Multiphase Flow, vol. 35(6), Kim S. et al. (2009), "Modeling of binary droplet collisions for application to inter-impingement sprays", pg. 533-549, Copyright (2020), with permission from Elsevier.*

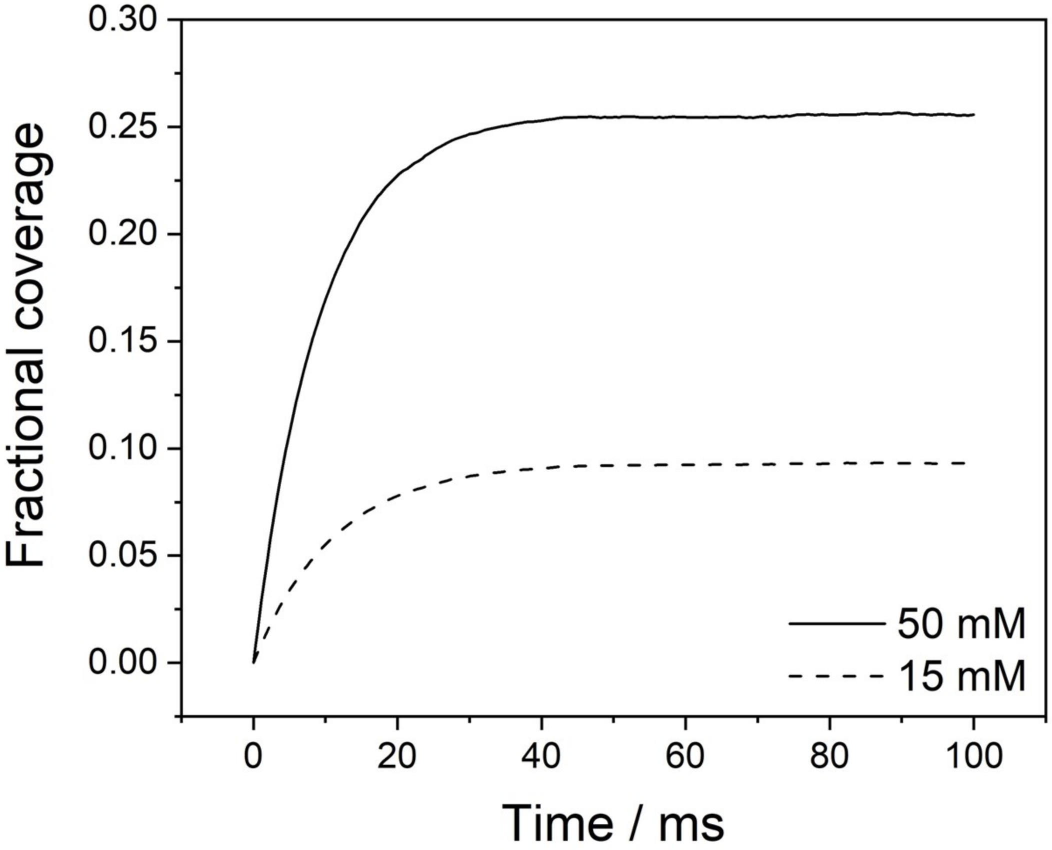

Figure S9: Kinetics of surface adsorption of pimelic acid acid (50 and 15 mM) in a 5 µm radius aqueous droplet. Calculations are done with the modelling framework presented by Wilson et al.,[26] *using the following parameters:* $k_{ads} = 9.3 \cdot 10^{-19}$ *cm*^{3} *molec.*$^{-1}$ *s*$^{-1}$*,* $k_{des} = 80$ *s*$^{-1}$*, molecular area = 30 A*^{2} *molec.*$^{-1}$*.*[27]

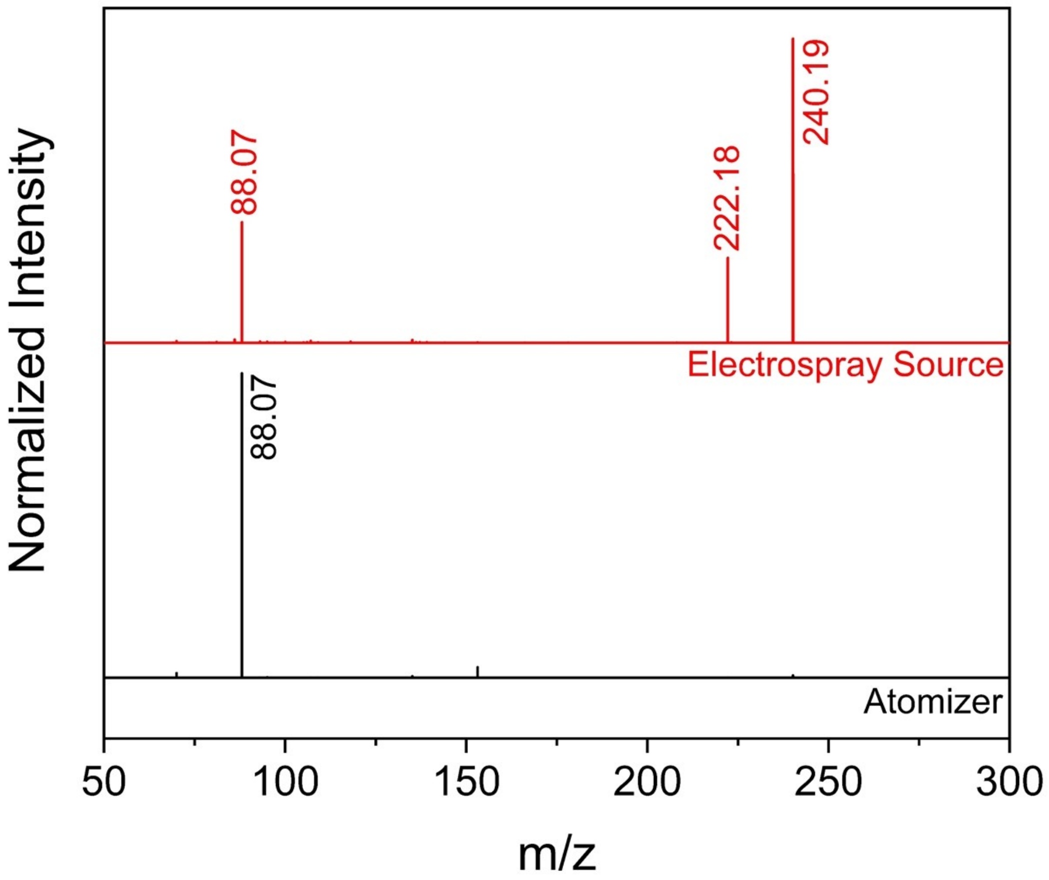

Figure S10: CID spectra of the product ion (m/z = 240.19, $[M+H^+]^+$*) from an ESSI source and from the atomizer experiments described in Section 4.8*

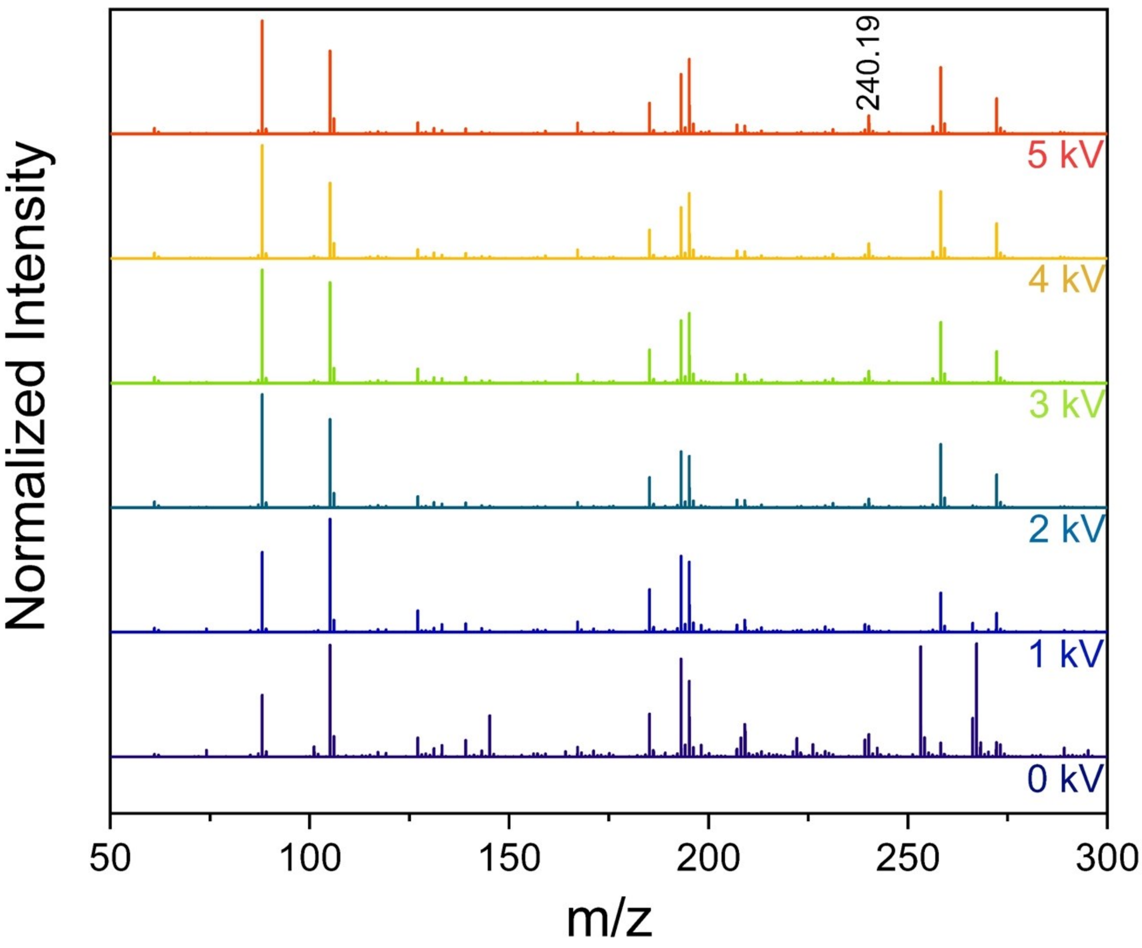

Figure S11: Mass spectra obtained from a mixture of morpholine and limonene oxide sprayed with an ESSI source, as a function of the applied voltage.

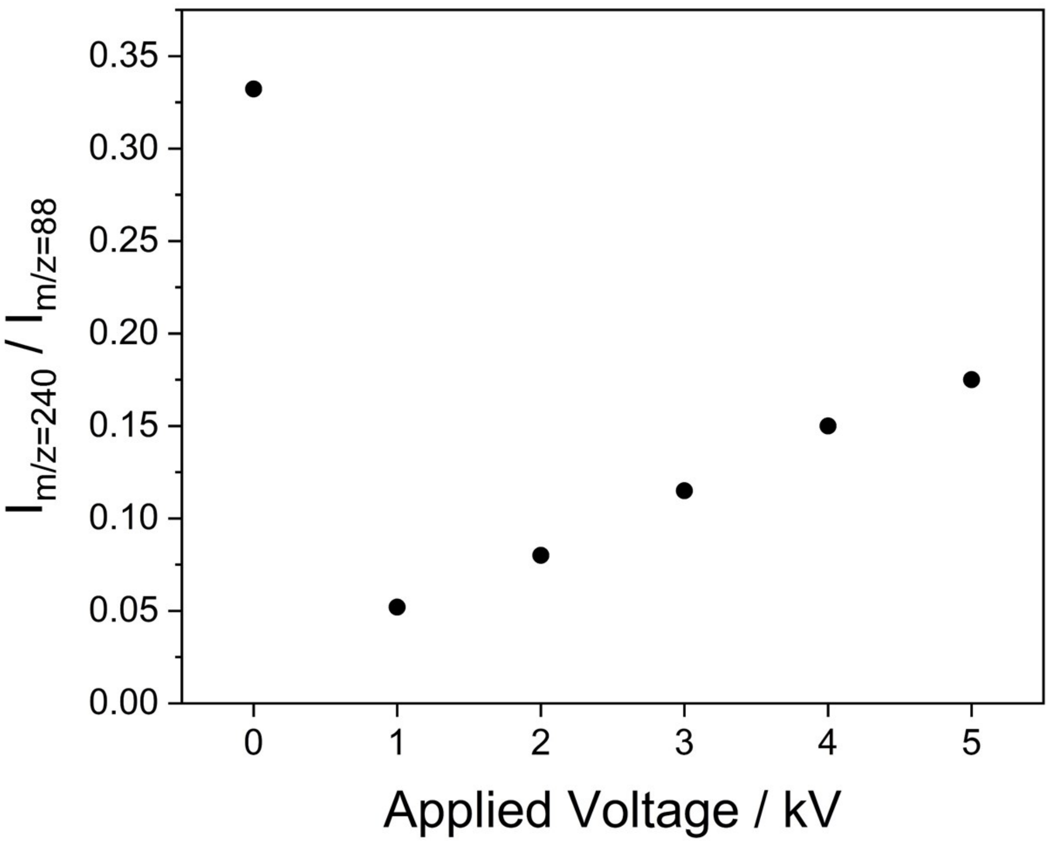

Figure S12: Ratio between the intensities of the peaks at m/z = 240.19 (product) and m/z = 88.07 (morpholine) as a function of the voltage applied to the ESSI source, extracted from the mass spectra in Figure S11. The trend agrees with findings in the work by Lai et al.[28] *(Figure 8 in their manuscript).*

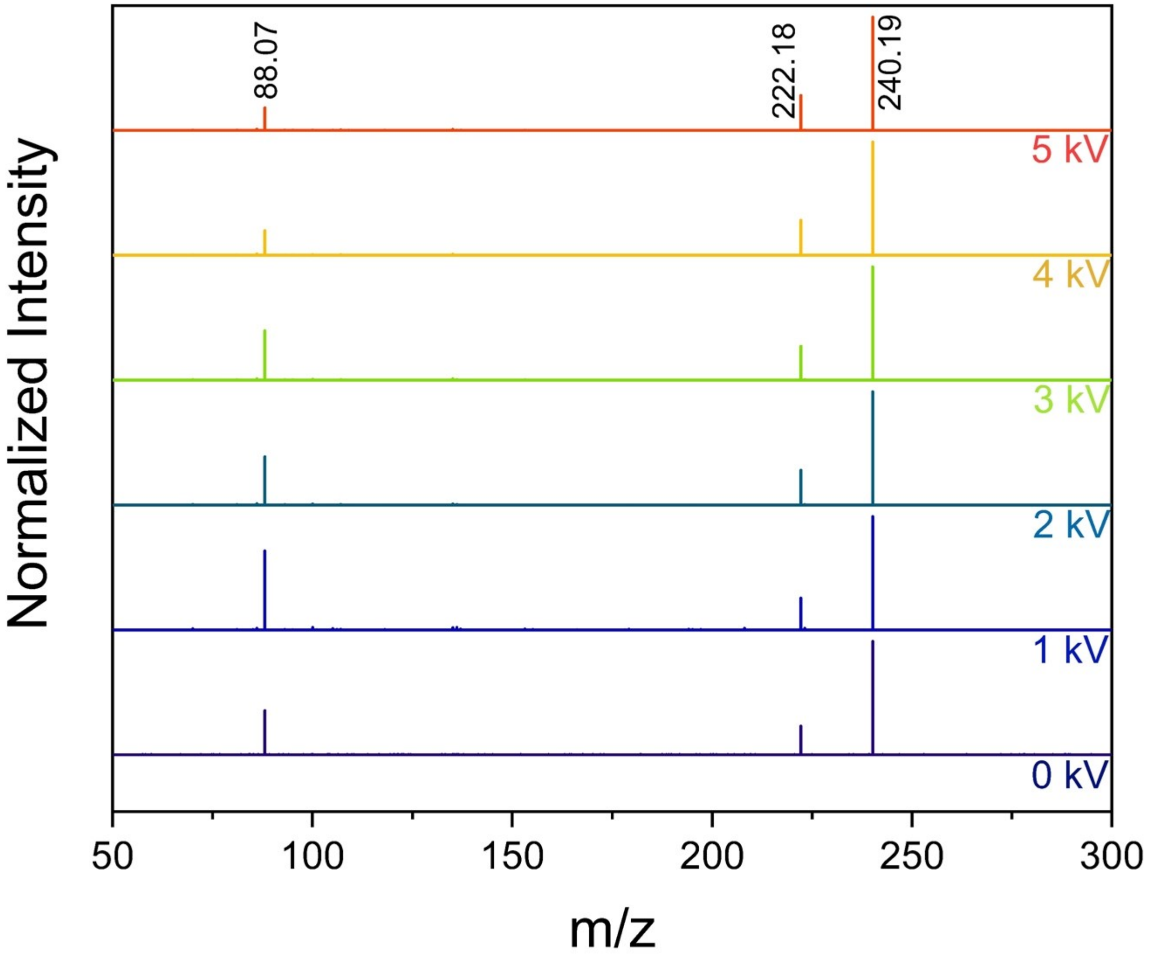

Figure S13: CID spectra of the product peak (m/z = 240.19) from the reaction of morpholine and limonene oxide obtained with the same applied voltage to the ESSI source as in Figure S11.

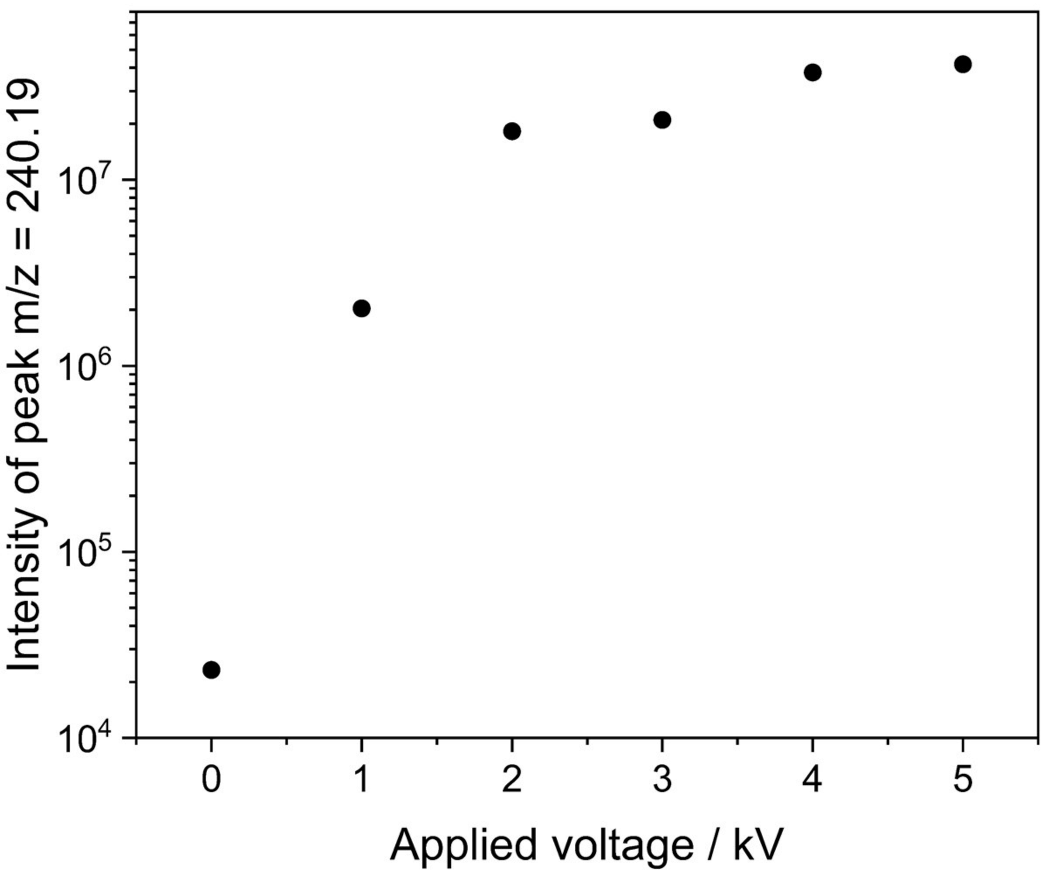

Figure S14: Raw ion counts for the peaks corresponding to the epoxide ring opening product at m/z = 240.19 in Figure S11, plotted against the voltage applied to the emitter tip.

m/z	**Ion**
229.06	$[Rib_2 -4H_2O +H^+]^+$
231.02	$[Rib+P -H_2O +H^+]^+$
245.07	$[Rib+U-H_2O+H^+]^+$
247.07	$[Rib_2 -3H_2O +H^+]^+$
249.03	$[Rib +P +H^+]^+$
263.08	$[Rib +Uracil +H^+]^+$
265.08	$[Rib_2 -2H_2O +H^+]^+$

Table S1: Peaks assignments for the uridine synthesis reaction in the mass spectra in Figure 8 of the main manuscript.

References:

1 E. J. Davis, *Adavnces Chem. Eng.*, 1992, **18**, 1–94.

2 F. K. A. Gregson, M. Ordoubadi, R. E. H. Miles, A. Haddrell, D. Barona, D. Lewis, T. Church, R. Vehring and J. P. Reid, *Phys. Chem. Chem. Phys.*, 2019, **21**, 9709–9719.

3 C. L. Yaws, *Handbook of Vapor Pressure. Volume 2 - C5 to C7 Compounds.*, Gulf Publishing Co., Houston, TX, 1994.

4 L. Tang and P. Kebarle, *Anal. Chem.*, 1993, **65**, 3654–3668.

5 J. A. Dean, *Lange's handbook of chemistry*, London: McGraw-Hill, Inc., New York., 1999.

6 S. Chapman and T. G. Cowling, *The mathematical theory of non-uniform gases: an account of the kinetic theory of viscosity, thermal conduction and diffusion in gases*, 1970.

7 M. J. Tang, M. Shiraiwa, U. Pöschl, R. A. Cox and M. Kalberer, *Atmos. Chem. Phys.*, 2015, **15**, 5585–5598.

8 D. M. Murphy and T. Koop, *Q. J. R. Meteorol. Soc.*, 2005, **131**, 1539–1565.

9 W. J. Massman, *Atmos. Environ.*, 1998, **32**, 1111–1127.

10 W. N. Haynes, *CRC Handbook of Chemistry and Physics, 6th ed.*, CRC Press, 2009.

11 M. J. O'Neil, Ed., *The Merck Index - An Encyclopedia of Chemicals, Drugs, and Biologicals.*, Merck and Co., Inc., Whitehouse Station, NJ, 13th Editi., 2001.

12 D. N. Mortensen and E. R. Williams, *J. Am. Chem. Soc.*, 2016, **138**, 3453–3460.

13 F. A. M. G. Van Geenen, M. C. R. Franssen, H. Zuilhof and M. W. F. Nielen, *Anal. Chem.*, 2018, **90**, 10409–10416.

14 Z. Olumee, J. H. Callahan and A. Vertes, *J. Phys. Chem. A*, 1998, **102**, 9154–9160.

15 J. K. Lee, S. Kim, H. G. Nam and R. N. Zare, *Proc. Natl. Acad. Sci. U. S. A.*, 2015, **112**, 3898–3903.

16 A. Stindt, C. Warschat, A. Bierstedt, U. Panne and J. Riedel, *Eur. J. Mass Spectrom.*, 2014, **20**, 21–29.

17 P. Nemes, I. Marginean and A. Vertes, *Anal. Chem.*, 2007, **79**, 3105–3116.

18 R. L. Grimm and J. L. Beauchamp, *J. Phys. Chem. A*, 2010, **114**, 1411–1419.

19 J. N. Smith, R. C. Flagan and J. L. Beauchamp, *J. Phys. Chem. A*, 2002, **106**, 9957–9967.

20 E. T. Jansson, Y.-H. Lai, J. G. Santiago and R. N. Zare, *JACS*, 2017, **139**, 6851−6854.

21 Y. H. Lai, S. Sathyamoorthi, R. M. Bain and R. N. Zare, *J. Am. Soc. Mass Spectrom.*, 2018, **29**, 1036–1043.

22 R. M. Bain, C. J. Pulliam, S. T. Ayrton, K. Bain and R. G. Cooks, *Rapid Commun. Mass Spectrom.*, 2016, **30**, 1875–1878.

23 B. M. Marsh, K. Iyer and R. G. Cooks, *J. Am. Soc. Mass Spectrom.*, 2019, **30**, 2022–2030.

24 R. D. Espy, A. R. Muliadi, Z. Ouyang and R. G. Cooks, *Int. J. Mass Spectrom.*, 2012, **325**–**327**, 167–171.

25 R. M. Bain, C. J. Pulliam, S. T. Ayrton, K. Bain and R. G. Cooks, *Rapid Commun. Mass Spectrom.*, 2016, **30**, 1875–1878.

26 K. R. Wilson, A. M. Prophet, G. Rovelli, M. D. Willis, R. J. Rapf and M. I. Jacobs, *Chem. Sci.*, 2020, **11**, 8533–8545.

27 G. Bleys and P. Joos, *J. Phys. Chem.*, 1985, **89**, 1027–1032.

28 Y. H. Lai, S. Sathyamoorthi, R. M. Bain and R. N. Zare, *J. Am. Soc. Mass Spectrom.*, 2018, **29**, 1036–1043.